Resonant ion acceleration by plasma jets: Effects of jet breaking and the magnetic-field curvature

A. V. Artemyev and A. A. Vasiliev
Space Research Institute (IKI) 117997, 84/32 Profsoyuznaya Str, Moscow, Russia
(Received 20 November 2014; revised manuscript received 17 January 2015; published 18 May 2015)

In this paper we consider resonant ion acceleration by a plasma jet originating from the magnetic reconnection region. Such jets propagate in the background magnetic field with significantly curved magnetic-field lines. Decoupling of ion and electron motions at the leading edge of the jet results in generation of strong electrostatic fields. Ions can be trapped by this field and get accelerated along the jet front. This mechanism of resonant acceleration resembles surfing acceleration of charged particles at a shock wave. To describe resonant acceleration of ions, we use adiabatic theory of resonant phenomena. We show that particle motion along the curved field lines significantly influences the acceleration rate. The maximum gain of energy is determined by the particle's escape from the system due to this motion. Applications of the proposed mechanism to charged-particle acceleration in the planetary magnetospheres and the solar corona are discussed.

DOI: 10.1103/PhysRevE.91.053104 PACS number(s): 52.20.Dq, 52.35.Vd, 94.05.Pt, 94.30.cl

I. INTRODUCTION

In numerous systems with strong plasma currents the magnetic reconnection drives a reconfiguration of the magnetic field topology and acceleration of charged particles. This is equally true for laboratory experiments [1,2], tokomaks [3], the near-Earth plasma environment [4–6], solar corona [7,8], magnetar [9] and pulsar [10] flares. Thus, charged-particle acceleration in the course of the magnetic reconnection is of general physical interest.

General configuration of the reconnection region implies the presence of cross-field electric currents localized within a relatively thin (small-scale) spatial domain (the so-called current sheet) [8]. At some distance from the reconnection site these currents support strong magnetic field gradients resulting in the magnetic field configuration with stretched field lines. Such configurations are observed by spacecraft in the planetary magnetospheres [11] and assumed to be formed in the solar corona [12] (see scheme in Fig. 1). Recent *in situ* spacecraft observations and modern numerical simulations of the magnetic reconnection suggest that a significant portion of magnetic energy stored in the current sheet can be realized in the form of fast plasma jets propagating from the reconnection site [13–16]. In both planetary magnetospheres and solar corona the reconnection jets are observed by direct [13,17,18] and indirect [19–21] measurements of plasma velocities and magnetic field perturbations. Propagation of such jets in an ambient plasma environment results in plasma heating and acceleration of charged particles [22,23]. Besides the heating of plasma [24–26] by electromagnetic field disturbances produced by jets (nonlinear structure of the magnetic field perturbation is often called a jet front, see scheme in Fig. 1), there is a nonadiabatic charged-particle acceleration due to the particle reflection from the front [27–29] or trapping by the front [30,31]. In the latter case, we deal with magnetic field perturbations of such strength that the jet creates a local secondary reconnection region where trapped particles are accelerated (see description of similar acceleration mechanisms in Refs. [32–34]).

The *in situ* spacecraft observations in the Earth magnetosphere give us a chance to investigate details of the jet front structure and dynamics [35–39]. Thus, information derived from the spacecraft observations can be used to construct models of charged-particle interaction with the jet front. Particularly, two interesting properties of the front structure and evolution were found recently: (1) the generation of Hall electric fields at the front [36,38] (the similar electric field was found in numerical simulations, see Ref. [40]); (2) the jet breaking [35,41,42]. The first property is related to the decoupling of electron and ion motions at the jet front where the magnetic field has a strong gradient (see scheme in Fig. 2). The jet breaking (i.e., the second property) results from the jet interaction with the strong background magnetic field in the close vicinity of the Earth. Influence of both these properties on charged-particle acceleration at the jet front were investigated: the strong electrostatic (Hall) field can trap particles at the front [43], while the front breaking results in the increase of efficiency of the particle acceleration [44,45]. Particle trapping by Hall electric field at the jet front in many aspects resembles the classical surfing mechanism of charged-particle trapping and acceleration at the shock wave [46–49].

However, in contrast to the plane shock geometry, there is a significant curvature of magnetic-field lines in the system with plasma jets (see the scheme in Fig. 3). Plasma jets originated from the magnetic-reconnection region propagate in the reconnected current sheet with strongly stretched magnetic-field lines [13,14]. Thus, field-line curvature can change particle trajectories essentially [50] and can influence efficiency of charged-particle acceleration by the jet front. In this paper we show that taking into account the field-line curvature in the model of charged-particle interaction with jets changes the character of the particle acceleration. We use an analytical approach to show that resonance conditions of charged-particle interaction with the jet front are satisfied for realistic system parameters. We estimate acceleration rate: energy of resonant particles grows with time as $\sqrt{t}$. Numerical integration of test-particle trajectories confirms the main predictions of the theory.

II. MODEL OF THE BACKGROUND MAGNETIC FIELD AND JET STRUCTURE

We consider a simple model describing curved field lines in the Earth magnetotail: $\mathbf{B} = B_0(z/L)\mathbf{e}_x + B_n\mathbf{e}_z$, where L is a

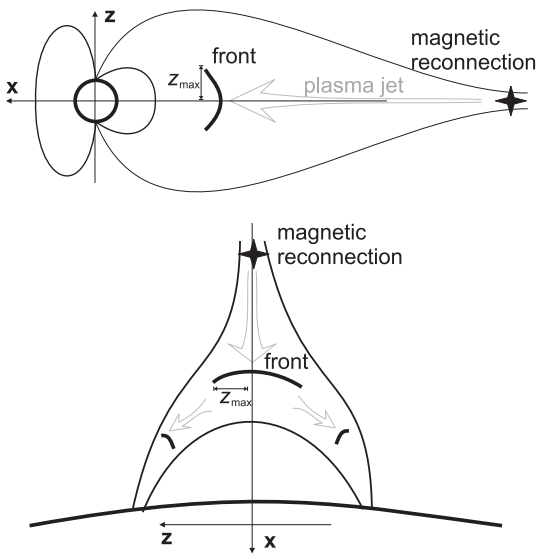

FIG. 1. Schematic view of formation of jet fronts in the planetary magnetosphere (top) and solar flare (bottom). Black curves show magnetic field lines.

current sheet thickness, B_0 and B_n are amplitudes of tangential and normal components of magnetic field (see scheme in Fig. 3). Note that the same configuration can be assumed to model charged-particle dynamics in flare magnetic loops in the solar corona [51,52]. Plasma jet moves from the deep magnetotail toward the Earth and the leading edge of the jet is characterized by strong increase of z component of the magnetic field. Thus, we describe this B_z-front by the magnetic field $B_w = \delta B_z f(\phi)\mathbf{e}_z$, where δB_z is an amplitude of the front magnetic field, function $f(\phi)$ describes the front shape, and phase ϕ is

$$\phi = \frac{1}{l_x}\left[x - \int^t v_\phi(\varepsilon t')dt'\right]. \tag{1}$$

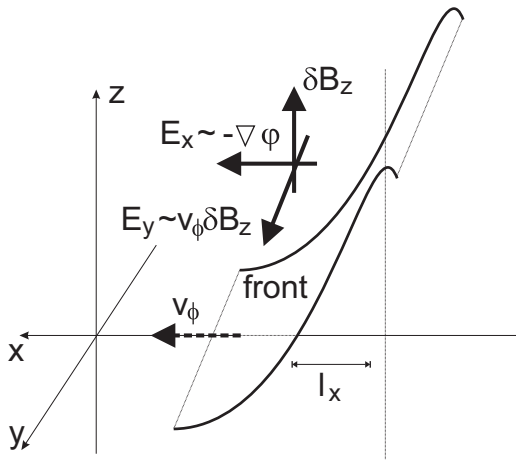

FIG. 2. Schematic view of the configuration of electric and magnetic fields at the front (φ is a scalar potential generated due to decoupling of ions and electron motions). The spatial scale of the front l_x is also shown.

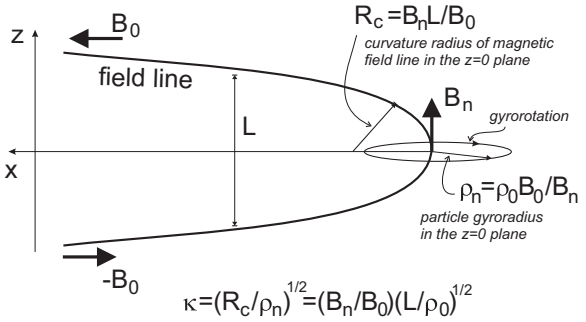

FIG. 3. Schematic view magnetic-field line and system parameters. Calculation of the κ parameter is shown.

In Eq. (1) the scale l_x corresponds to the front scale (see scheme in Fig. 2), while function $v_\phi(t)$ describes the dependence of the front velocity on slow time εt with $\varepsilon \ll 1$ (we introduce this dependence to model the front breaking process [42,53]). The total vector potential (background and front) has only one nonzero component,

$$A_y = B_n x - B_0 \frac{z^2}{2L} + \delta A_y(\phi), \tag{2}$$

where

$$\frac{\partial \delta A_y}{\partial \phi} = l_x \frac{\partial \delta A_y}{\partial x} = l_x \delta B_z f(\phi). \tag{3}$$

Propagation of the front through the ambient plasma results in generation of strong electrostatic field E_x (see scheme in Fig. 2) directed normally to the front [38,39,54]. Simple analytical estimates of this field can be obtained from the stress balance [43]:

$$E_x = -\sigma B_n \frac{df^2}{d\phi}, \tag{4}$$

where we take into account that $\delta B_z \gg B_n$, σ is a normalized amplitude of the electric field: $\sigma = (\max E_x/B_n)\chi$, $\chi \in [0,1]$ determines the contribution of electrons to the current density at the front. Strictly speaking, $\max E_x$ depends on the ratio of δB_z^2 and plasma density, but we do not specify this dependence and use σ as a free parameter. The corresponding scalar potential is

$$\varphi(\phi) = \sigma l_x B_n f^2(\phi). \tag{5}$$

There are several models describing charged-particle interaction with jet fronts or strong electromagnetic waves. Each model assumes a specific form of the $f(\phi)$ function: the function $f = \sin\phi$ is used to simulate charged-particle acceleration by strong wavelike structure of electromagnetic field [32,34]; the simple steplike function $f = (1/2)[1 - \tanh(\phi)]$ simulates well the front configuration [27,55,56]; 2D modifications of front profile with $f = f(z,\phi)$ were considered in Refs. [31,57]; localized electromagnetic pulses with $f(\phi) \to 0$ for $|\phi| \gg 1$ were considered in Refs. [29,30]. To demonstrate influence of front breaking and electrostatic fields onto charged-particle acceleration in the system with curved magnetic-field lines, we choose a simple front profile $f = (1/2)[1 - \tanh(\phi)]$. Profiles of f, f^2 (scalar potential), and $df^2/d\phi$ (electrostatic field) are shown in Fig. 4.

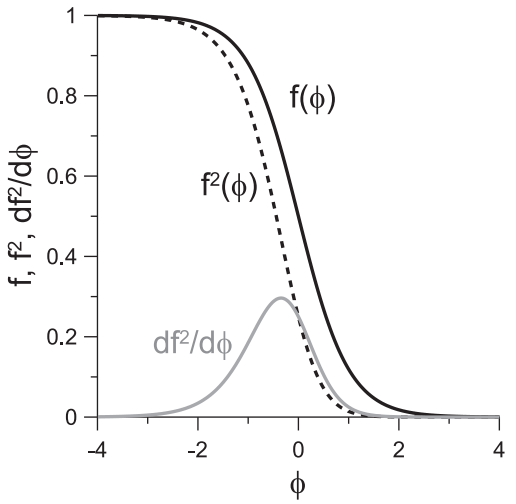

FIG. 4. Profiles of $f(\phi)$, $f^2(\phi)$, and $df^2/d\phi$ functions.

In this paper we use system parameters typical for the near-Earth magnetotail (75–90 thousands of km from the Earth): magnetic field $\delta B_z \sim 10$–30 nT [36], $l_x \sim 100$–1000 km [22,36], background magnetic field $B_n \sim 0.1$–10 nT [58,59] and $B_0 \sim 30$ nT [35,60], $L \sim 1000$–10000 km [15,61]. Parameter χ is often close to one, i.e., almost all electric current is carried by electrons, [62], while max E_x reaches 10–100 mV/m [15,38]. Thus, parameter σ is about ~ 0.01–0.1.

III. ION MOTION: ANALYTICAL EQUATIONS

We start with the Hamiltonian of an ion with charge e and mass m:

$$H = \frac{1}{2m}\left(\mathbf{P} - \frac{e}{c}\mathbf{A}\right)^2 + e\varphi(\phi) = \frac{P_x^2 + P_z^2}{2m} + e\varphi(\phi) + \frac{1}{2m}\left\{P_y - \frac{e}{c}\left[B_n x - B_0\frac{z^2}{2L} + \delta A_y(\phi)\right]\right\}^2, \quad (6)$$

where $\mathbf{A}$ and φ are vector and scalar potentials, $\mathbf{P}$ is the particle's momentum, (x,z) are the particle's coordinates. Hamiltonian Eq. (6) does not depend on y coordinate; thus, $P_y = \text{const}$ and we can set $P_y = 0$. This procedure corresponds to the shift of the coordinate system $x \to x + cP_y/eB_n$ and the shift of phase ϕ by a constant value $\phi_0 = cP_y/l_x eB_n$. This shift does not change the system because Hamiltonian Eq. (6) contains only linear terms $\sim x$. We introduce dimensionless variables $(x,z)/\sqrt{\rho_0 L} \to (x,z)$, $\mathbf{P}/mv_0 \to \mathbf{P}$, $tv_0/\rho_0 \to t$, $H/mv_0^2 \to H$, where v_0 is an amplitude of the particle velocity, and $\rho_0 = v_0 mc/eB_0$. In the new variables, Hamiltonian Eq. (6) takes the form

$$H = \frac{1}{2}\left(P_x^2 + P_z^2\right) + \frac{e\varphi(\phi)}{mv_0^2} + \frac{1}{2}\left(\kappa x - \frac{1}{2}z^2 + \frac{\delta A_y(\phi)}{\rho_0 B_0}\right)^2, \quad (7)$$

where $\kappa = (B_n/B_0)\sqrt{L/\rho_0}$. This parameter determines the ratio of the scale of the magnetic-field inhomogeneity (the curvature of magnetic-field line) and the maximum value of particle gyroradius (gyroradius calculated at the plane $z = 0$); see the scheme in Fig. 3. Two terms $\sim \delta A_y, \varphi$ in Eq. (7) can be rewritten as

$$\frac{\delta A_y(\phi)}{\rho_0 B_0} = \frac{\delta B_z l_x}{\rho_0 B_0}F(\phi) = \kappa\frac{\delta B_z}{B_n}L_x F(\phi) = \kappa\ell F(\phi),$$
$$\frac{e\varphi(\phi)}{mv_0^2} = \frac{el_x B_n \sigma f^2(\phi)}{mv_0^2} = \kappa\frac{cL_x}{v_0}\sigma f^2(\phi) = \kappa\Phi(\phi), \quad (8)$$

where $F(\phi) = \int f d\phi$, $\Phi = \bar{\sigma} f^2(\phi)$, $\ell = \delta B_z L_x/B_n$, and $\bar{\sigma} = \sigma c L_x/v_0$. We also introduce dimensionless scale $L_x = l_x/\sqrt{L\rho_0}$. Thus, the final form of Hamiltonian Eq. (7) is

$$H = \frac{1}{2}\left(P_x^2 + P_z^2\right) + \kappa\Phi(\phi) + \frac{1}{2}\left\{\frac{1}{2}z^2 - \kappa[x + \ell F(\phi)]\right\}^2. \quad (9)$$

Hamiltonian Eq. (9) describes the system with $2\frac{1}{2}$ degrees of freedom: $H = H(x,P_x,z,P_z,t)$, where t is included into ϕ according to Eq. (1). Instead of time dependence we would like to introduce ϕ as a new variable to get an autonomous system. This procedure can be performed in two steps [63]. At the first step we introduce nonlinear time $\psi = L_x^{-1}\int^t v_\phi(\varepsilon t')dt'$ and canonically conjugated momentum P_ψ. To preserve the equations of motion, the term $v_\phi(\varepsilon t)P_\psi/L_x$ should be added to Hamiltonian Eq. (9). Parameter ε is the smallest parameter in the system and, thus, time εt changes much slower than all other variables. Strictly speaking, the transformation of time t to phase ψ should also result to change of εt to a function of ψ. However, all variations of function v_ϕ with ψ are of the order of $\varepsilon \ll 1$. Thus, we neglect these variations and consider $\tau = \varepsilon t$ as a system parameter.

The transformation from t to ψ is not a canonical transformation as the number of variables is increased [from (x,P_x,z,P_z,t) to $(x,P_x,z,P_z,\psi,P_\psi)$]. However, the obtained autonomous Hamiltonian $N = H + v_\phi P_\psi/L_x$ properly describes the same dynamical system as Hamiltonian Eq. (9), as it gives the same equations of motion for all the variables (P_x,x,P_z,z,t) [63]. The second step corresponds to introduction of the phase ϕ as a new canonical variable. This is done through the canonical transformation with generating function R depending on old coordinates and new momenta,

$$R = I\left(\frac{x}{L_x} - \psi\right) + p_x x + p_z z; \quad (10)$$

thus, $P_\psi = -I$. We keep notations (x,z) for the new coordinates and rewrite Hamiltonian Eq. (9) in the new variables as

$$F = \frac{1}{2}\left(p_x + \frac{I}{L_x}\right)^2 + \frac{1}{2}p_z^2 + \frac{1}{2}\left\{\frac{1}{2}z^2 - \kappa[x + \ell F(\phi)]\right\}^2 - \Omega I + \kappa\Phi(\phi), \quad (11)$$

where $\Omega = v_\phi/L_x$, ϕ is an independent variable, I is a variable canonically conjugated with ϕ, and the new momenta are

$$p_x = P_x - I/L_x, \quad p_z = P_z. \quad (12)$$

Autonomous Hamiltonian Eq. (11) depends on variables (x,p_x,z,p_z) and on phase ϕ calculated along the particle's trajectory, while variable I does not have particular physical meaning. The following procedure of consideration of resonance assumes that we separate Hamiltonian Eq. (11) in two parts: one part depends on fast oscillation phase ϕ, while the other part does not depend on ϕ. The separate consideration of dynamics of these two parts allows us to describe oscillations of phase ϕ in a vicinity of the resonance and the corresponding evolution of slow variables [64]. However, before this separation can be performed, we average system Eq. (11) over the fastest oscillations in the plane (z,p_z).

We introduce h_z as

$$h_z = \tfrac{1}{2}p_z^2 + \tfrac{1}{2}\left\{\tfrac{1}{2}z^2 - \kappa[x+\ell F(\phi)]\right\}^2. \tag{13}$$

The z motion is faster than variations of ϕ and κx, thus we can average over z oscillations [65,66]. This averaging gives

$$F = -\Omega I + \kappa\Phi(\phi) + \frac{1}{2}\left(p_x + \frac{I}{L_x}\right)^2 + h_z(\zeta,I_z), \tag{14}$$

where $I_z = \oint p_z dz \approx \text{const}$ is the adiabatic invariant and

$$\zeta = \xi + \kappa\ell F(\phi), \quad h_z(\zeta) \approx h_z(\xi) + \kappa\ell h_z'(\xi)F(\phi). \tag{15}$$

In Eq. (15), $\xi = \kappa x$, $h_z' = dh_z/d\xi$. Thus, Hamiltonian Eq. (14) takes the form

$$\begin{aligned} F &= F_0(p_x,\xi,I) + \kappa F_1(\xi,\phi),\\ F_0 &= -\Omega I + \frac{1}{2}\left(p_x + \frac{I}{L_x}\right)^2 + h_z(\xi),\\ F_1 &= \Phi(\phi) + \ell h_z'(\xi)F(\phi), \end{aligned} \tag{16}$$

where conjugated variables are (I,ϕ) and $(p_x,\kappa^{-1}\xi)$. Equations of motion for Hamiltonian Eq. (16) are

$$\begin{aligned} \dot I &= -\frac{\partial F}{\partial\phi} = -\kappa[\Phi'(\phi) + \ell h_z'(\xi)f(\phi)],\\ \dot\phi &= \frac{\partial F}{\partial I} = -\Omega + \frac{1}{L_x}\left(p_x + \frac{I}{L_x}\right),\\ \dot p_x &= -\kappa\frac{\partial F}{\partial\xi} = -\kappa h_z'(\xi) + O(\kappa^2),\\ \dot\xi &= \kappa\frac{\partial F}{\partial p_x} = \kappa\left(p_x + \frac{I}{L_x}\right). \end{aligned} \tag{17}$$

Equation (17) show that variables (ξ,p_x) are slow (a variation rate of these variables is about $\sim\kappa \ll 1$), while phase ϕ changes with the rate ~ 1. Thus, one can average the system over fast oscillations of ϕ. This averaging procedure gives $\dot I = 0$, i.e., I is an adiabatic invariant of full system Eq. (17) and is conserved exactly in the system averaged over ϕ oscillations. This averaging works well everywhere except for a close vicinity of the resonance $\dot\phi = 0$, where the variation rate of ϕ drops to zero. Thus, at the resonance we expect to obtain a variation of I.

The resonance condition $\dot\phi = 0$ gives $p_x + I/L_x = \Omega L_x$. We introduce the resonant value of the invariant $I_R = L_x(\Omega L_x - p_x)$. The isoenergetic surface (where $F_0 = h$ and h is the particle's energy) in (p_x,ξ,I) space is

$$h = -\Omega I + \frac{1}{2}\left(p_x + \frac{I}{L_x}\right)^2 + h_z(\xi). \tag{18}$$

To study dynamics near the resonance, we follow the standard approach developed in Refs. [67,68]. We expand Hamiltonian Eq. (16) near the resonance $I = I_R$:

$$F = \Lambda(p_x,\xi) + \tfrac{1}{2}g(I-I_R)^2 + \kappa F_1|_{I=I_R}, \tag{19}$$

where

$$\kappa F_1|_{I=I_R} = \kappa\ell h_z'(\xi)F(\phi) + \kappa\Phi(\phi), \tag{20}$$

and

$$\begin{aligned} \Lambda = F_0|_{I=I_R} &= -\Omega I_R + \frac{1}{2}\left(p_x + \frac{I_R}{L_x}\right)^2 + h_z(\xi)\\ &= \Omega L_x\left(p_x - \frac{1}{2}\Omega L_x\right) + h_z(\xi). \end{aligned} \tag{21}$$

To deduce Eq. (21) we substituted $I_R = I_R(p_x,\xi)$ to Eq. (16). Factor g in Eq. (19) is

$$g = \left.\frac{\partial^2 F_0}{\partial I^2}\right|_{I=I_R} = \frac{1}{L_x^2}. \tag{22}$$

We introduce a new variable $K = I - I_R + O(\kappa)$ through a canonical transformation with the generation function

$$Q = p_X\kappa^{-1}\xi + (K+I_R)\phi. \tag{23}$$

In the new variable, the new Hamiltonian G is

$$\begin{aligned} G &= \Lambda(p_X,X) + \mathcal{F}(K,\phi,X,\tau),\\ \mathcal{F} &= \frac{1}{2L_x^2}K^2 + \kappa[\ell h_z'(X)F(\phi) + \Phi(\phi)]\\ &\quad + \kappa\left[L_x h_z'(X) + \frac{\varepsilon}{\kappa}L_x^2\frac{\partial\Omega}{\partial\tau}\right]\phi, \end{aligned} \tag{24}$$

where $\tau = \varepsilon t$ and we consider $\Omega = v_\phi/L_x$ again as a function of slow time εt. Thus, Hamiltonian G depends on $\Omega(\tau)$ and is not autonomous. We keep notation ϕ for the phase variable conjugated with K;

$$X = \xi + \frac{\partial I_R}{\partial p_X}\kappa\phi \tag{25}$$

is the new variable conjugated with κp_X (note that $p_X = \kappa\partial Q/\partial X = \partial Q/\partial x = p_x$).

Equation (24) shows that we divide initial Hamiltonian Eq. (9) into a combination of two Hamiltonians. The Hamiltonian Λ describes particle trajectories in the 2D surface generated by the intersection of 3D surface Eq. (18) and 2D resonant surface $I = I_R$. The second Hamiltonian $\mathcal{F}$ describes oscillations of fast-phase ϕ around the resonant trajectory. Note that (p_X,X) in Eq. (24) are slow variables. Strictly speaking, Hamiltonian Λ also depends on slow-time τ. However, rate of change of this slow time $\sim\varepsilon$ is much smaller than the rate of change of (p_X,X) variables. Thus, we consider Hamiltonian $\Lambda(p_X,X)$ as a one-dimensional Hamiltonian depending on system parameter τ. The more accurate approach would give us corrections of the order of $\varepsilon \ll 1$. We omit these corrections. The following numerical simulations of

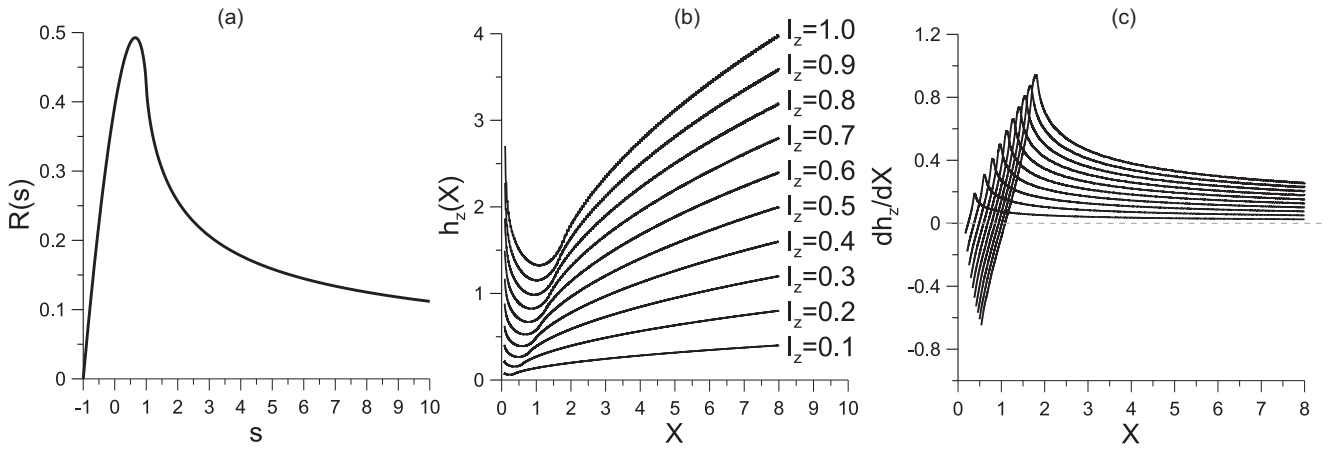

FIG. 5. (a) The profile of the $R(s)$ function given by Eq. (30). (b) The profiles of $h_z(X)$ for various values of I_z. (c) The profiles of $h_z'(X)$ for various values of I_z.

full system justify this approach. Thus, to describe particle dynamics in the vicinity of the resonance we first consider the Hamiltonian $\mathcal{F} = (1/2)gK^2 + \kappa W(X,\phi) + \kappa b(X,\varepsilon t)\phi$, with

$$W = \ell h_z'(X)F(\phi) + \Phi(\phi),$$
$$b = L_x h_z'(X) + L_x^2 \frac{\varepsilon}{\kappa}\frac{\partial \Omega}{\partial \tau}. \tag{26}$$

In this case, the presence of a potential minimum in Hamiltonian $\mathcal{F}$ is given by the two conditions: (1) an extremum of the potential exists if for some ϕ one can get $\dot{K} = 0$; (2) this extremum is the potential minimum if $d^2(\ell h_z' F + \Phi)/d\phi^2 > 0$. Both conditions can be written as

$$\left(\ell h_z'(X) + 2\bar{\sigma}\frac{df}{d\phi}\right) f(\phi) + b = 0,$$
$$\left(q\frac{\delta B_z}{B_n}h_z' + \frac{df}{d\phi}\right)\frac{df}{d\phi} + f\frac{d^2 f}{d\phi^2} > 0, \tag{27}$$

where $q = L_x/2\bar{\sigma}$.

We rewrite Eq. (27) as

$$\left(q\frac{\delta B_z}{B_n}h_z' + \frac{df}{d\phi}\right) f(\phi) + q\left(h_z' + \frac{\varepsilon}{\kappa}\frac{\partial L_x \Omega}{\partial \tau}\right) = 0. \tag{28}$$

To determine the behavior of relation Eq. (28) with variation of ϕ one needs to define $h_z'(X)$ profile. The function $h_z(X)$ can be obtained from the equation $I_z = \text{const}$, where

$$I_z = \frac{1}{2\pi}\oint p_z dz$$
$$= \frac{1}{2\pi}\oint \sqrt{2h_z - \left(\frac{1}{2}z^2 - \kappa(x + \ell F(\phi))\right)^2}\, dz. \tag{29}$$

Equation (29) implies that $I_z = (2h_z)^{3/4}R(s)$ with

$$s = (X + \kappa\ell F(\phi) + \kappa L_x\phi)/\sqrt{2h_z},$$
$$R(s) = \frac{1}{\pi}\int_{\tilde{z}_-}^{\tilde{z}_+}\sqrt{1 - \left(s - \frac{1}{2}\tilde{z}^2\right)^2}\, d\tilde{z}. \tag{30}$$

The profile $R(s)$ is shown in Fig. 5 (left panel). Inverting function $R(s)$ we can plot h_z as a function of X (here we neglect small terms $\kappa\ell F + \kappa L_x\phi$). Figure 5 (central panel) shows nonmonotonical $h_z(X)$ profiles obtained for several I_z values. At large X the function h_z increases as $\sqrt{X}$ (the asymptote $R(s) \sim 1/\sqrt{s}$ at $s \gg 1$; see Ref. [69]). Using profiles $h_z(X)$ we plot $h_z'(X)$ in Fig. 5 (right panel). There is a local maximum of h_z' and then h_z' monotonically decreases with X [66].

Now we can substitute the dependence $h_z'(X)$ into Eq. (28) and plot a 2D map showing a range of X values where solutions of Eq. (28) exist for a given value of q. We choose a simple profile $\Omega(\tau) = \Omega_0(1 - \tau)$ and introduce dimensionless parameter $u_\phi = -L_x\Omega_0\varepsilon/\kappa$. Figure 6 shows that particles cannot be trapped at small X. At higher values of I_z the trapping becomes possible only for small q.

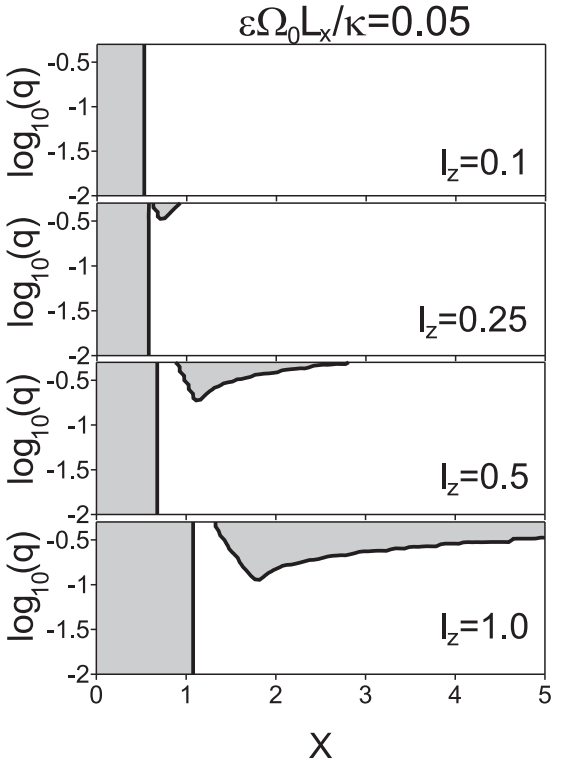

FIG. 6. Map in the (X,q) plane: the gray color shows regions where Eq. (28) does not have a solution for given values of parameters.

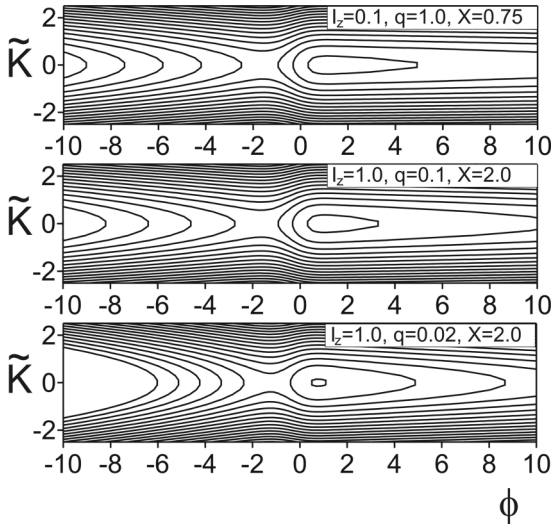

FIG. 7. Three phase portraits of Hamiltonian Eq. (26) for three sets of parameters. Here $\tilde{K} = K/L_x\sqrt{\kappa\bar{\sigma}}$.

Figure 6 shows that there are regions of X values where condition Eq. (27) can be satisfied. For these regions the phase portraits of Hamiltonian $\mathcal{F}$ in the (K,ϕ) plane are shown in Fig. 7. One can see the domain filled by closed phase trajectories in the phase plane. Particles moving along these trajectories are trapped. One can calculate the area of this domain $S = \oint K d\phi$, as

$$S(X) = 2^{3/2}L_x \int_{\phi_m}^{\phi_s} \sqrt{\mathcal{F} - \kappa W(X,\phi) - \kappa b(X,\tau)\phi}\, d\phi$$
$$= 2^{3/2}\kappa^{1/2}L_x \times \int_{\phi_m}^{\phi_s} \sqrt{W(\phi_s) + b(\tau)\phi_s - W(\phi) - b(\tau)\phi}\, d\phi, \quad (31)$$

where ϕ_s is a solution of equations $dW/d\phi = -b$, while ϕ_m is a solution of equation

$$W(\phi_s) + b\phi_s - W(\phi) - b\phi = 0. \quad (32)$$

For the simplified case $\Omega(\tau) = \Omega_0(1-\tau)$ we plot profiles $S(X)$ in Fig. 8 (upper panel). If area S grows along the particle trajectories, new particles can be trapped into the region filled by closed trajectories [67,68]. Thus, Fig. 8 (upper panel) shows that X should increase along trajectories of potentially trapped particles.

In the trapped motion particle's coordinates (X, p_X) vary according to Hamiltonian equations with Hamiltonian Λ given by Eq. (21):

$$\kappa\dot{p}_X = -\frac{\partial\Lambda}{\partial X} = -h_z', \quad \dot{X} = \kappa\frac{\partial\Lambda}{\partial p_X} = \kappa\Omega L_x. \quad (33)$$

Figure 8 shows that trapping (i.e., the growth of S) is possible only when h_z' decreases. Thus, trapped particles move with velocity $\dot{X} = \kappa\Omega L_x$ and decreasing p_X. In this case, particle acceleration [growth of Λ; see Eq. (21)] is possible only if the term $h_z(X)$ increases along the trajectory more significantly than the term $\sim\Omega L_x(p_x - \Omega L_x)$ decreases. This condition is satisfied for trapped particles. Indeed, Fig. 5 shows that $h_z(X)$

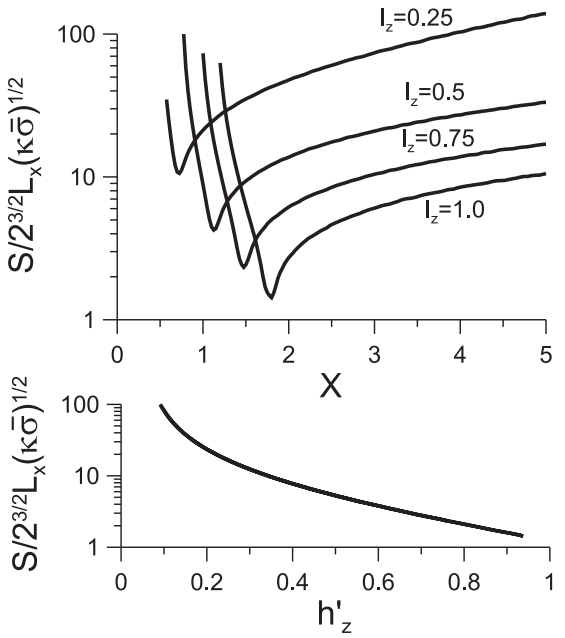

FIG. 8. Profiles of $S(X)$ and $S(h_z')$ normalized on $2^{2/3}L_x\sqrt{\kappa\bar{\sigma}}$ for several values of I_z.

increases as $\sim\sqrt{X}$ at large enough values of X. Therefore, for trapped particles we expect to obtain energy growth $\sim\sqrt{X}$ with $X(t)$ given by Eq. (33).

IV. ION MOTION: TEST PARTICLE RESULTS

To check the effect of particle trapping and acceleration by a breaking front we numerically integrate Hamiltonian equations for Hamiltonian Eq. (9). Two particle trajectories are shown in Figs. 9 and 10.

Initial part of the particle trajectories (before interaction with the front) are shown with gray color. These are typical particle trajectories in the current sheet—particles rotate along almost closed curves described by equation $I_z(X,p_x) =$ const [65,69,70]. There is a separatrix in the (z,p_z) plane [and corresponding uncertainty curve in the (X,p_x) plane], and each crossing of this separatrix results in a small $\sim\kappa$ jump of I_z [50,71]. These jumps slowly destroy closed trajectories in the (X,p_x) plane and a particle drifts from one trajectory (corresponding to a certain value of I_z) to another trajectory. One can find corresponding variations of I_z with time in the right top panels of both Figs. 9 and 10. Roughly speaking, after averaging over z oscillations (i.e., after introduction of the I_z invariant) we deal with 2D particle motion in the plane (X,p_x) along closed trajectories and a slow drift between these trajectories. The time scale of the particle motion in the (X,p_x) plane is $\sim 1/\kappa$ [this is a scaling of the quasi-period of particle motion in the (X,p_x) plane], while the time scale of particle drift between trajectories is $1/\kappa^3$ [50,69].

When a particle is trapped by the front, it starts moving with the front: the particle coordinate κX increases, while p_x oscillates around $v_\phi(t)$ value (see trajectories and right panels in Figs. 9 and 10). Trajectories of trapped particles in the (X,p_x) plane look like sets of rapid jumps in p_x

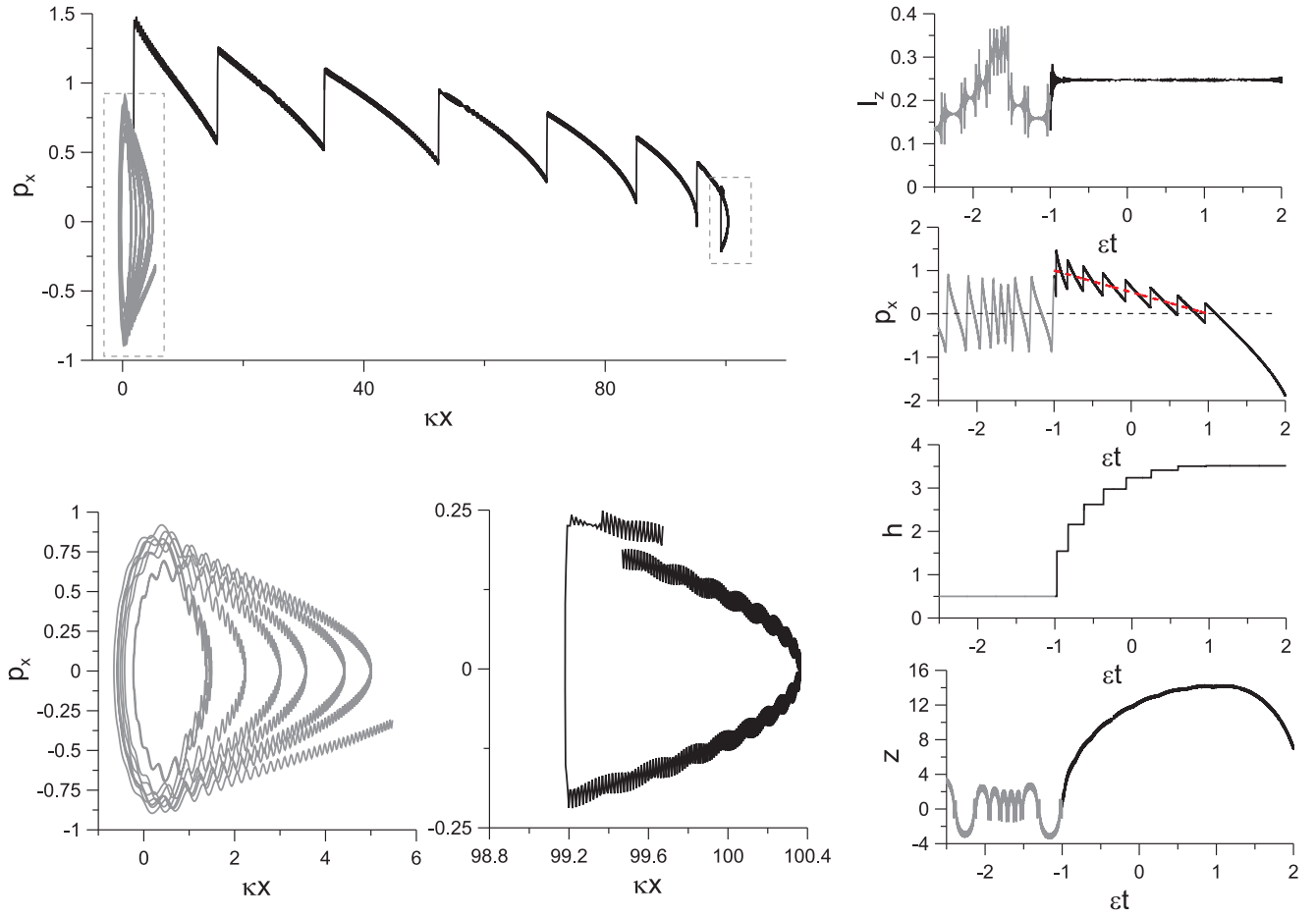

FIG. 9. (Color online) Particle trajectory in $(\kappa x, p_x)$ plane (the gray color shows the trajectory segment before the trapping); two additional panels show trajectory fragments before the trapping and after escape from the resonance. Right panels show time profiles of I_z invariant, p_x component of the particle momentum, particle energy, and z coordinate. Red dotted line shows profiles of $v_\phi(t)$. System parameters are: $\kappa = 0.1$, $\varepsilon = 0.01$, $\delta B_z/B_n = 3$, $L_x = 0.1$.

followed by slow decreases. These are oscillations in the trapped state. Each of these oscillations corresponds to a jump of the particle energy. Moreover, the front shifts particles to higher $|z|$. Thus, the resonant acceleration resembles the betatron acceleration mechanism: a trapped particle moves with the front along X with velocity $v_\phi(t)$ and is propelled by the front toward the region with stronger magnetic field (magnetic-field amplitude is $\sim|z|$). A similar mechanism of charged-particle acceleration was found earlier for ion acceleration by moving magnetic-field reversal [e.g., 57,66] and for relativistic electron acceleration by whistler waves [e.g., 72,73]. Panels with particle energy $h(\varepsilon t)$ in Figs. 9 and 10 show that energy $h = h_z + p_x^2/2$ grows despite the decrease of p_x. Thus, the main particle acceleration is provided by the increase of $h_z(\kappa x)$.

There are two possible scenarios of escape from the resonance: (1) the field breaking of the front (i.e., the front velocity v_ϕ drops to zero) and (2) the particle reaching the boundary of the current sheet (i.e., $|z| \to z_{\max}$). In our modeling we consider the rapid breaking of the front; thus, particles escape from the resonance when v_ϕ becomes zero. After escaping from the resonance, particles start moving along typical trajectories (similar to trajectories before the trapping).

V. DISCUSSION AND CONCLUSIONS

Before discussing the obtained results and comparing them with spacecraft observations we would like to compare main predictions of our model with other theoretical models of charged-particle acceleration by plasma jet fronts. Self-consistent kinetic model of jet-front formation and evolution shows that at these fronts ion currents can effectively dissipate magnetic-field energy [14,54]. The direct investigation of charged-particle acceleration is performed using one of two approaches: (1) electromagnetic-field configuration of the front can be derived from self-consistent MHD simulation and then these fields are used in the test particle approach [24,74]; or (2) particles are traced in prescribed electromagnetic field imitating the configuration of the jet front [27,29,31,56]. The first approach allows us to use relatively realistic dynamics of electromagnetic field in the course of plasma jet propagation toward the Earth, while the second approach gives a chance to model a fine structure of front configuration unavailable in MHD simulations.

Interaction of electrons with jet fronts obtained in MHD modeling is almost adiabatic [75] and, thus, is well reproduced in the framework of guiding center approximation [74]. Although, ion dynamics in such models is significantly

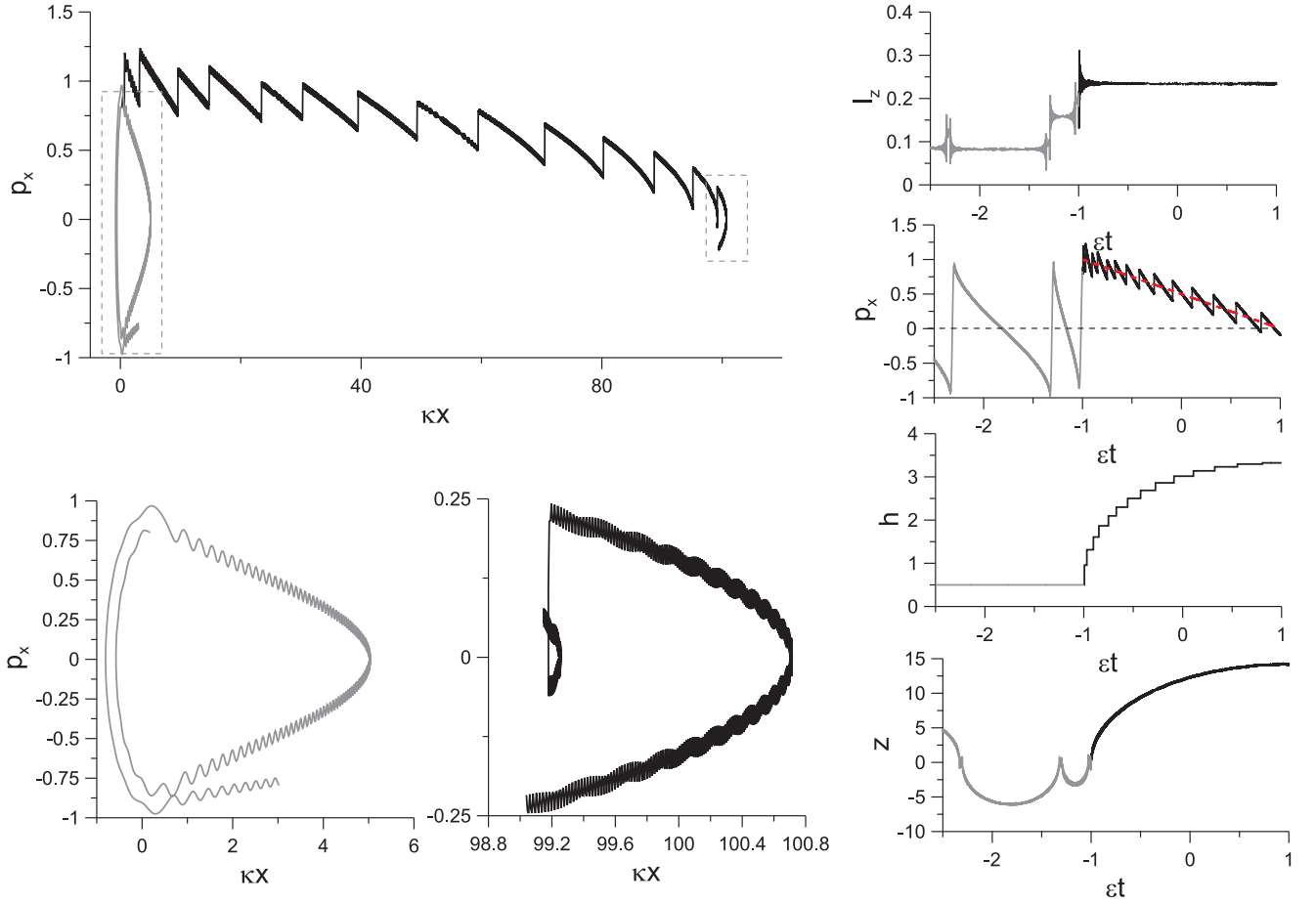

FIG. 10. (Color online) Particle trajectory in $(\kappa x, p_x)$ plane (the grey color shows the trajectory segment before the trapping); two additional panels show trajectory fragments before the trapping and after escape from the resonance. Right panels show time profiles of I_z invariant, p_x component of the particle momentum, particle energy, and z coordinate. Red dotted line shows profiles of $v_\phi(t)$. System parameters are: $\kappa = 0.1$, $\varepsilon = 0.01$, $\delta B_z/B_n = 3$, $L_x = 0.01$.

nonadiabatic, the efficiency of ion acceleration is very close to the efficiency of electron acceleration [74]. Thus, in both cases we deal with the acceleration due to particle drifts in inhomogeneous magnetic field along the front (some analog of betatron and Fermi mechanisms).

In case of ion tracing in prescribed magnetic-field configuration imitating a jet front, the main acceleration mechanism (in the absence of resonant effects) corresponds to particle reflection from the front [27,56]. Although such reflection is a nonadiabatic process, there is a simplified geometrical model of the corresponding particle acceleration [76]: particle interaction with a moving front can be considered as an elastic reflection of a ball from the moving wall. This acceleration mechanism resembles particle reflection from a shock wave [77]. Thus, the mechanism proposed in this paper can be considered as a generalization of simple particle reflection from the front for systems with electrostatic potential responsible for the particle trapping.

The numerical integration of charged-particle trajectories (see Figs. 9 and 10) demonstrates two interesting features of the charged-particle resonant interaction with the jet front. First of all, trapped particles move with the front and pass a long distance along the x axis. Thus, in addition to the acceleration we observe transport of charged particles. This is an especially important effect if we consider the ion interaction with jet fronts in the near-Earth magnetotail. In this region jets are believed to be responsible for injections of charged particles from the outer magnetosphere into the radiation belts [44,78,79]. Thus, our model shows one additional mechanism for the charged-particle transport across the magnetic field B_z in the important region of the Earth magnetosphere.

The second feature corresponds to the charged-particle acceleration during its motion along curved field lines. As particle velocity along the x axis coincides with the front velocity, all acceleration is due to the growth of other components of the particle momentum. The particle motion along field lines with fixed $p_x \approx v_\phi$ means the increase of X coordinate as $X \approx \int^t v_\phi(\tilde{t})d\tilde{t}$. This increase of X coordinate corresponds to particle motion toward the region with stronger magnetic field, because particles propagate along the field lines with $|z| \sim \sqrt{2X}$ and $|B_x| \sim |z|$. Thus, the particle energy grows as $\sim|z|$ (like in betatron acceleration). The similarity of $|z|$ and $h(t)$ profiles is well seen in Figs. 9 and 10. It should be mentioned that a similar acceleration mechanism is working for magnetized particles (when I_z can be replaced by the magnetic moment) trapped by strong electromagnetic or electrostatic waves in the current sheet [80,81]. Thus, we have shown that taking into account the curvature of

magnetic-field lines significantly modifies the resonant mechanism of charged-particle acceleration by the jet front. Instead of classical surfing acceleration along the front, particles escape from the minimum-$|\mathbf{B}|$ region and move along field lines. This modification changes the acceleration rate: instead of the ballistic acceleration with $h \sim t^2$ [30,32,55], we obtain betatron-like acceleration rate with $h \sim h_z \sim \sqrt{t}$. Moreover, particle motion along field lines can effectively limit the maximum gain of energy. For surfing acceleration this gain is about the potential drop $\sim\Delta\Phi$ across the front [46,47], while particles escaping the system at the top bottom boundaries $|z| \to z_{\max}$ can gain only $h \sim h_z(X_{\max})$ with $X_{\max} \approx z_{\max}^2/2$ (see scheme in Fig. 1).

The estimate of maximum gained energy $h_{\max} \approx h_z(X_{\max}) \approx 1.4\sqrt{X_{\max}} \approx z_{\max}$ (see Fig. 5 for approximation $h_z(X_{\max}) \approx 1.4\sqrt{X_{\max}}$ given for large I_z; $z_{\max}$ is shown in the scheme in Fig. 1) can be rewritten in dimensional form as $h_{\max}/h_0 \approx \sqrt{L/\rho_0}$, where $h_0 = mv_0^2/2$ is an initial energy and L is a thickness of the depolarized current sheet, i.e., the current sheet region located far from the reconnection region. (To derive this equation we use back transformation to dimensional variables $z_{\max} \to z_{\max}/\sqrt{L\rho_0} = \sqrt{L/\rho_0}$ with $z_{\max} \approx L$; i.e., there is no plasma jet above and below the current sheet region.) Using this simple estimate we can predict the efficiency of the proposed acceleration mechanism for various plasma systems. We consider three magnetospheres (Earth, Mercury, and Jupiter) where plasma jets and the corresponding fronts were observed by spacecraft [13,17,18]. We also consider parameters typical for solar flares [7,82] and for reconnection in solar wind [5,83,84]. For the most investigated Earth magnetosphere we separately consider near-Earth magnetotail (region at the night-side with $x > -10^5$ km, see the scheme in Fig. 1 for the direction of x axis), and the distant magnetotail ($x < -1.5 \times 10^5$ km). For each system we estimate acceleration of thermal protons (H^+), cold particles (for planetary magnetospheres these are protons with the energy of the solar wind plasma; for solar wind we consider protons not heated in the reconnection region), and heavy ions (for each system we choose corresponding ion species). Table I gives the information about system parameters, initial energies of particles, estimates of ratio L/ρ_0, and final energy.

In the near-Earth magnetotail plasma jet fronts originate from the near-Earth X-line region [85] and propagate toward the Earth until breaking at the boundary of the inner magnetosphere where Earth dipole magnetic field dominates [42]. The thickness of surrounding current sheet and magnetic-field amplitudes B_0 are about $\sim$6400 km (i.e., one Earth radius) and $\sim$40 nT [86,87], correspondingly. Temperature of thermal protons is about 10 keV [88], while cold protons penetrating from the flank magnetosphere have energy about 1 keV [89]. Oxygen ions escaping from the ionosphere are heated up to energies $\sim$10 keV comparable with the energy of thermal protons [90]. Interaction of these three types of particles with jets front produces the following effects: thermal protons and oxygen ions are accelerated up to superthermal energies $\sim$20–40 keV, while cold protons gain $\sim$8 keV and reach the temperature of the thermal population. The generated population of superthermal protons and oxygen ions are indeed observed in the jet-breaking region where these ions contribute significantly to formation of the current system of the inner magnetosphere [91] and to generation of ultralow frequency waves [92,93].

In the distant Earth magnetotail the current sheet is thicker than in the near-Earth region ($L > 12\,000$ km; see Ref. [94]), while magnetic-field amplitude is about $\sim$10 nT [95]. Plasma jets with related fronts are often observed in this region (e.g., Refs. [96,97]) and are associated to the local reconnection process or plasma transport from the near-Earth X line. Temperature of thermal protons in the distant tail is about $\sim$3 keV [95,98], while cold protons have the energy $\sim$1 keV. One of the main population of heavy ions is represented by He^{++} penetrating from the solar wind (where these ions can represent up to 10% of the plasma content [99]) or generated by interaction of solar wind protons and the Moon surface [100]. Our estimates show that thermal protons and He^{++} ions can be accelerated up to 10 keV, while cold protons gain energy around $\sim$5 keV. Such high-energy He^{++} ions are really detected in the near-Earth region [101,102] where they are drifted due to magnetoshere plasma convection from the distant tail. The superthermal protons $\sim$10 keV can contribute to population of high-energy particle beams observed in the distant magnetotail near the reconnection region [103].

The Mercury magnetosphere is much more compact and dynamical than the Earth magnetosphere due to stronger solar wind influence and smaller planetary magnetic field [11,104]. The typical current sheet thickness in the Mercury magnetotail is about $\sim$2500 km (i.e., about the Mercury radius), while magnetic-field amplitude is about $\sim$50 nT [105,106]. Strong perturbation of Mercury magnetosphere by solar wind transients results in frequent magnetic reconnection [107] and formation of plasma jets with the corresponding fronts [17]. Thermal protons and heavy ions in the Mercury magnetotail

TABLE I. Main parameters and efficiency of charged-particle acceleration in various plasma systems.

	Parameters	Thermal H^+			Cold plasma			Heavy ions			
System	L and B_0 1000 km and nT	h_0 keV	L/ρ_0	$h_{\max}$ keV	h_0 keV	L/ρ_0	$h_{\max}$ keV	type	h_0 keV	L/ρ_0	$h_{\max}$ keV
Near-Earth	$L \sim 6.4$, $B_0 \sim 40$	10	$\sim$18	40	1	$\sim$58	8	O^+	10	$\sim$5	20
Distant Earth	$L > 12$, $B_0 \sim 10$	3	$\sim$17	12	1	$\sim$29	5	He^{++}	4	$\sim$10	12
Mercury	$L \sim 2.5$, $B_0 \sim 50$	2.5	$\sim$20	10	1	$\sim$29	5	Na^+	1	$\sim$6	2.5
Jupiter	$L > 140$, $B_0 \sim 15$	10	$\sim$150	120	1	$\sim$480	22	S^+	45	$\sim$22	160
Solar flares	$L \sim 10^{-4}$, $B_0 \sim 10^6$	0.1	$\sim$70	1				Mg^{+9}	0.1	$\sim$130	1.2
Solar wind	$L \sim 0.5$, $B_0 \sim 10$	0.02	$\sim$8	0.06	0.005	$\sim$16	0.02	He^{++}	0.05	$\sim$5	0.11

(e.g., Na^+) have energies around ∼2.5 and ∼1 keV [108], while cold solar wind protons have energy ∼1 keV. Table I shows that cold protons can be accelerated up to thermal energies, while acceleration of thermal protons and heavy ions result in formation of high-temperature population ∼10 keV (and ∼2.5 keV) also observed in the Mercury magnetotail (see discussion in Refs. [108–110]).

Due to the strong planetary magnetic field and weak solar wind the Jupiter magnetosphere is much larger than the Earth magnetosphere [11]. The magnetotail region with characteristic stretched field lines is located at the distance $\sim 3.5 \times 10^6$ km from the Jupiter (e.g., at 50 Jupiter radii). Thickness of the current sheet at such distance is about $\sim 1.4 \times 10^5$ km, while magnetic-field amplitude is $B_0 \sim 15$ nT [111]. Spacecraft observations often detect in this region various signatures of magnetic reconnection [112,113] and the corresponding fronts of plasma jets [18,114]. The plasma content in this region represents the mixture of protons with energy ∼10 keV and sulfur ions S^+ with energy ∼45 keV [115,116], while cold plasma of the solar wind penetrating into distant magnetotail should have energy around ∼1 keV. Table I shows that the proposed mechanism results in thermal proton acceleration up to ∼120 keV, while S^+ ions are accelerated up to ∼160 keV. Indeed, the increase of fluxes of such high-energy protons and ions are observed in a vicinity of jet fronts in the Jupiter magnetotail [57]. Acceleration of cold protons up to ∼20 keV can be considered as an additional source of the thermal plasma.

The recorded x-ray emission from solar flares allows us to assume that the magnetic reconnection of the current sheet located above the loop is responsible for magnetic energy release and charged-particle acceleration [7]. Although system parameters for current sheets in solar corona are less known (in comparison with planetary magnetospheres), we present estimates of the efficiency of the proposed acceleration mechanism in Table I. We use characteristic values of the current sheet thickness $L \sim 100$ m and magnetic-field amplitude $B_0 \sim 10^6$ nT [52,82]. Temperature of thermal protons is taken ∼0.1 keV (we do not consider cold population of ions for this system) [7,82]. To estimate the efficiency of acceleration of heavy ions we consider ions Mg^{+9} observed in solar corona by SoHO spacecraft [117,118]. Table I shows that protons and heavy ions can be accelerated by fronts of plasma jets up to 1 keV. This is rather small energy of particles in flare events, thus, we conclude that trapping and acceleration of protons by plasma jet fronts can be effective only in case of multiple interactions with several jets. It is interesting to note that some models of ion acceleration in solar flares assume the presence of multireconnection with formation of many X lines and the corresponding plasma jets [119,120].

The last system that we consider is the heliospheric current sheet in the vicinity of the reconnection region. In contrast to previously described systems (planetary magnetospheres and solar corona), the main energy of charged particles in solar wind corresponds to the bulk velocity of solar wind, while charged-particle temperatures are rather low (about ∼10 eV). The magnetic reconnection in the heliospheric current sheet takes place in the region with current sheet thickness about ∼500 km, while magnetic-field amplitude is about ∼10 nT [83,84]. Initial temperatures of cold solar wind is ∼5 eV, while temperature of protons heated at the reconnection region is ∼20 eV [5]. Heavy ions He^{++} have temperatures ∼50 eV [99]. Table I shows that cold protons can be accelerated up to energies ∼20 eV observed at the vicinity of the reconnection region [5]. Acceleration of hot protons and heavy ions up to 60–100 eV can contribute to the nonthermal population solar wind [121,122].

Estimates shown in Table I demonstrate that the proposed acceleration mechanism can effectively increase energy of cold plasma content up to thermal energies, while the efficiency of acceleration of initially hot particles depends on system configuration. In the planetary magnetospheres plasma jets can be responsible for generation of high-energy proton and ion populations with energies comparable to the data of spacecraft observations.

Our model is essentially based on the adiabatic theory assuming conservation of the adiabatic invariant of fast-particle oscillations in the background magnetic field. Introduction of this invariant allows us to decrease the number of degrees of freedom in the system. This reduced system can be expanded in a vicinity of the resonance; thus, one separates the charged-particle motion along the resonance surface from fast oscillations of the resonance phase. This is a rather common approach for description of Hamiltonian systems with the passage through the resonance [67,68]. Thus, our model contains two averaging procedures: (1) the introduction of the adiabatic invariant I_z often used to describe the charged-particle motion in current sheets [50] and (2) averaging over fast oscillations of the resonant phase ϕ (i.e., introduction of invariant I). This double averaging gives us a chance to explain the particle dynamics analytically.

To conclude, we have considered a nonrelativistic charged-particle motion in the system with curved magnetic-field lines and the breaking plasma jet. We have shown that strong electrostatic fields at the jet front can create a local potential minimum for positively charged particles (ions). Trapping into such a potential minimum results in the resonant acceleration of charged particles moving with the jet. Timescale of charged-particle acceleration is limited by the timescale of the jet-breaking. In many respects such trapping and acceleration resemble the classical surfing acceleration at shock waves, but the effect of curved field lines significantly changes dynamics of trapped particles.

ACKNOWLEDGMENTS

The authors are thankful to Prof. A. Neishtadt for fruitful discussions. We also thank the reviewers for their valuable comments. The work was supported by the Russian Scientific Foundation (Project No. 14-12-00824).

[1] M. Yamada, R. Kulsrud, and H. Ji, Rev. Modern Phys. **82**, 603 (2010).

[2] A. G. Frank, Phys. Uspekhi **53**, 941 (2010).

[3] A. H. Boozer, Phys. Plasmas **19**, 058101 (2012).

[4] J. Birn and E. R. Priest, *Reconnection of Magnetic Fields: Magnetohydrodynamics and Collisionless Theory and Observations*, edited by J. Birn and E. R. Priest (Cambridge University Press, Cambridge, 2007).

[5] J. T. Gosling, Space Sci. Rev. **172**, 187 (2012).

[6] G. Paschmann, M. Øieroset, and T. Phan, Space Sci. Rev. **178**, 385 (2013).

[7] M. J. Aschwanden, Space Sci. Rev. **101**, 1 (2002).

[8] E. Priest and T. Forbes, *Magnetic Reconnection* (Cambridge University Press, Cambridge, 2000), p. 612.

[9] Y. Masada, S. Nagataki, K. Shibata, and T. Terasawa, Pub. Astronom. Soc. Japan **62**, 1093 (2010).

[10] J. Arons, Space Sci. Rev. **173**, 341 (2012).

[11] C. M. Jackman, C. S. Arridge, N. André, F. Bagenal, J. Birn, M. P. Freeman, X. Jia, A. Kidder, S. E. Milan, A. Radioti, J. A. Slavin, M. F. Vogt, M. Volwerk, and A. P. Walsh, Space Sci. Rev. **182**, 85 (2014).

[12] S. Masuda, T. Kosugi, H. Hara, S. Tsuneta, and Y. Ogawara, Nature (London) **371**, 495 (1994).

[13] A. Runov, V. Angelopoulos, M. I. Sitnov, V. A. Sergeev, J. Bonnell, J. P. McFadden, D. Larson, K. Glassmeier, and U. Auster, Geophys. Res. Lett. **36**, L14106 (2009).

[14] M. I. Sitnov, M. Swisdak, and A. V. Divin, J. Geophys. Res. **114**, A04202 (2009).

[15] A. Runov, V. Angelopoulos, and X.-Z. Zhou, J. Geophys. Res. **117**, A05230 (2012).

[16] H. S. Fu, J. B. Cao, Y. V. Khotyaintsev, M. I. Sitnov, A. Runov, S. Y. Fu, M. Hamrin, M. André, A. Retinò, Y. D. Ma, H. Y. Lu, X. H. Wei, and S. Y. Huang, Geophys. Res. Lett. **40**, 6023 (2013).

[17] T. Sundberg, J. A. Slavin, S. A. Boardsen, B. J. Anderson, H. Korth, G. C. Ho, D. Schriver, V. M. Uritsky, T. H. Zurbuchen, J. M. Raines, D. N. Baker, S. M. Krimigis, R. L. McNutt, Jr., and S. C. Solomon, J. Geophys. Res. **117**, A00M03 (2012).

[18] S. Kasahara, E. A. Kronberg, T. Kimura, C. Tao, S. V. Badman, A. Masters, A. Retinò, N. Krupp, and M. Fujimoto, J. Geophys. Res. **118**, 375 (2013).

[19] H. Hara, T. Watanabe, L. K. Harra, J. L. Culhane, and P. R. Young, Astrophys. J. **741**, 107 (2011).

[20] S. Takasao, A. Asai, H. Isobe, and K. Shibata, Astrophys. J. Lett. **745**, L6 (2012).

[21] Y. Su, A. M. Veronig, G. D. Holman, B. R. Dennis, T. Wang, M. Temmer, and W. Gan, Nature Phys. **9**, 489 (2013).

[22] V. Angelopoulos, A. Runov, X. Z. Zhou, D. L. Turner, S. A. Kiehas, S. S. Li, and I. Shinohara, Science **341**, 1478 (2013).

[23] J. F. Drake, M. Swisdak, P. A. Cassak, and T. D. Phan, Geophys. Res. Lett. **41**, 3710 (2014).

[24] M. Ashour-Abdalla, M. El-Alaoui, M. L. Goldstein, M. Zhou, D. Schriver, R. Richard, R. Walker, M. G. Kivelson, and K.-J. Hwang, Nature Phys. **7**, 360 (2011).

[25] J. Birn, A. V. Artemyev, D. N. Baker, M. Echim, M. Hoshino, and L. M. Zelenyi, Space Sci. Rev. **173**, 49 (2012).

[26] H. S. Fu, Y. V. Khotyaintsev, A. Vaivads, A. Retinò, and M. André, Nature Phys. **9**, 426 (2013).

[27] X.-Z. Zhou, Y. S. Ge, V. Angelopoulos, A. Runov, J. Liang, X. Xing, J. Raeder, and Q.-G. Zong, J. Geophys. Res. **117**, A10227 (2012).

[28] X.-Z. Zhou, V. Angelopoulos, A. Runov, J. Liu, and Y. S. Ge, J. Geophys. Res. **117**, A10216 (2012).

[29] A. Greco, A. V. Artemyev, and G. Zimbardo, J. Geophys. Res. **119**, 8929 (2014).

[30] A. V. Artemyev, V. N. Lutsenko, and A. A. Petrukovich, Ann. Geophys. **30**, 317 (2012).

[31] A. Y. Ukhorskiy, M. I. Sitnov, V. G. Merkin, and A. V. Artemyev, J. Geophys. Res. **118**, 4952 (2013).

[32] S. Takeuchi, K. Sakai, M. Matsumoto, and R. Sugihara, Phys. Lett. A **122**, 257 (1987).

[33] S. Takeuchi, Phys. Plasmas **19**, 070703 (2012).

[34] A. I. Neishtadt, A. V. Artemyev, L. M. Zelenyi, and D. L. Vainshtein, JETP Lett. **89**, 441 (2009).

[35] R. Nakamura, A. Retinò, W. Baumjohann, M. Volwerk, N. Erkaev, B. Klecker, E. A. Lucek, I. Dandouras, M. André, and Y. Khotyaintsev, Ann. Geophys. **27**, 1743 (2009).

[36] A. Runov, V. Angelopoulos, X.-Z. Zhou, X.-J. Zhang, S. Li, F. Plaschke, and J. Bonnell, J. Geophys. Res. **116**, A05216 (2011).

[37] D. Schmid, M. Volwerk, R. Nakamura, W. Baumjohann, and M. Heyn, Ann. Geophys. **29**, 1537 (2011).

[38] H. S. Fu, Y. V. Khotyaintsev, A. Vaivads, M. André, and S. Y. Huang, Geophys. Res. Lett. **39**, L06105 (2012).

[39] M. A. Balikhin, A. Runov, S. N. Walker, M. Gedalin, I. Dandouras, Y. Hobara, and A. Fazakerley, J. Geophys. Res. **119**, 6367 (2014).

[40] M. I. Sitnov, N. Buzulukova, M. Swisdak, V. G. Merkin, and T. E. Moore, Geophys. Res. Lett. **40**, 22 (2013).

[41] R. Nakamura, W. Baumjohann, E. Panov, M. Volwerk, J. Birn, A. Artemyev, A. A. Petrukovich, O. Amm, L. Juusola, M. V. Kubyshkina, S. Apatenkov, E. A. Kronberg, P. W. Daly, M. Fillingim, J. M. Weygand, A. Fazakerley, and Y. Khotyaintsev, J. Geophys. Res. **118**, 2055 (2013).

[42] J. Liu, V. Angelopoulos, X.-Z. Zhou, and A. Runov, J. Geophys. Res. **119**, 909 (2014).

[43] A. V. Artemyev, G. Zimbardo, A. Y. Ukhorskiy, and M. Fujimoto, Astron. Astrophys. **562**, A58 (2014).

[44] C. Gabrielse, V. Angelopoulos, A. Runov, and D. L. Turner, J. Geophys. Res. **117**, A10213 (2012).

[45] A. V. Artemyev, Phys. Rev. E **89**, 033108 (2014).

[46] M. Gedalin, J. Geophys. Res. **101**, 4871 (1996).

[47] M. A. Lee, V. D. Shapiro, and R. Z. Sagdeev, J. Geophys. Res. **101**, 4777 (1996).

[48] G. P. Zank, H. L. Pauls, I. H. Cairns, and G. M. Webb, J. Geophys. Res. **101**, 457 (1996).

[49] A. A. Vasiliev, in *Advance in Plasma Physics* (Nova Science Publishers, Hauppauge, NY, 2002), Vol. 5, pp. 129–132.

[50] L. M. Zelenyi, A. I. Neishtadt, A. V. Artemyev, D. L. Vainchtein, and H. V. Malova, Phys. Uspekhi **56**, 347 (2013).

[51] T. Terasawa, K. Shibata, and M. Scholer, Adv. Space Res. **26**, 573 (2000).

[52] K. K. Reeves, T. B. Guild, W. J. Hughes, K. E. Korreck, J. Lin, J. Raymond, S. Savage, N. A. Schwadron, H. E. Spence, D. F. Webb, and M. Wiltberger, J. Geophys. Res. **113**, A00B02 (2008).

[53] V. A. Sergeev, I. A. Chernyaev, V. Angelopoulos, A. V. Runov, and R. Nakamura, Geophys. Res. Lett. **41**, 1106 (2014).

[54] M. I. Sitnov and M. Swisdak, J. Geophys. Res. **116**, A12216 (2011).

[55] S. Takeuchi, Phys. Plasmas **12**, 102901 (2005).

[56] X.-Z. Zhou, V. Angelopoulos, V. A. Sergeev, and A. Runov, J. Geophys. Res. **115**, A00I03 (2010).

[57] A. V. Artemyev, S. Kasahara, A. Y. Ukhorskiy, and M. Fujimoto, Planet. Space Sci. **82-83**, 134 (2013).

[58] J. R. Kan and W. Baumjohann, Geophys. Res. Lett. **17**, 271 (1990).

[59] A. V. Artemyev, A. A. Petrukovich, R. Nakamura, and L. M. Zelenyi, Ann. Geophys. **31**, 1109 (2013).

[60] V. A. Sergeev, D. G. Mitchell, C. T. Russell, and D. J. Williams, J. Geophys. Res. **98**, 17345 (1993).

[61] A. V. Artemyev and L. M. Zelenyi, Space Sci. Rev. **178**, 419 (2013).

[62] X.-J. Zhang, V. Angelopoulos, A. Runov, X.-Z. Zhou, J. Bonnell, J. P. McFadden, D. Larson, and U. Auster, J. Geophys. Res. **116**, A00I20 (2011).

[63] A. Neishtadt, A. Vasiliev, and A. Artemyev, Moscow Math. J. **11**, 531 (2011).

[64] V. I. Arnold, V. V. Kozlov, and A. I. Neishtadt, *Mathematical Aspects of Classical and Celestial Mechanics*, 3rd ed., Dynamical Systems III. Encyclopedia of Mathematical Sciences (Springer-Verlag, New York, 2006).

[65] J. Büchner and L. M. Zelenyi, Phys. Lett. A **118**, 395 (1986).

[66] D. L. Vainchtein, E. V. Rovinsky, L. M. Zelenyi, and A. I. Neishtadt, J. Nonlin. Sci. **14**, 173 (2004).

[67] A. I. Neishtadt, *Hamiltonian Systems with Three or More Degrees of Freedom*, NATO ASI Series C Vol. 533 (Kluwer Academic Publishers, Dordrecht, 1999), pp. 193–213.

[68] A. I. Neishtadt and A. A. Vasiliev, Nucl. Instrum. Methods Phys. Res. A **561**, 158 (2006).

[69] J. Büchner and L. M. Zelenyi, J. Geophys. Res. **94**, 11821 (1989).

[70] J. Chen, J. Geophys. Res. **97**, 15011 (1992).

[71] A. I. Neishtadt, Soviet J. Plasma Phys. **12**, 568 (1986).

[72] A. Artemyev, V. Krasnoselskikh, O. Agapitov, D. Mourenas, and G. Rolland, Phys. Plasmas **19**, 122901 (2012).

[73] A. Osmane and A. M. Hamza, Nonlin. Proc. Geophys. **21**, 115 (2014).

[74] J. Birn, M. Hesse, R. Nakamura, and S. Zaharia, J. Geophys. Res. **118**, 1960 (2013).

[75] J. Birn, M. F. Thomsen, and M. Hesse, Phys. Plasmas **11**, 1825 (2004).

[76] S. W. H. Cowley and P. Shull Jr., Planet. Space Sci. **31**, 235 (1983).

[77] R. B. Decker, Space Sci. Rev. **48**, 195 (1988).

[78] X. Li, D. N. Baker, M. Temerin, G. D. Reeves, and R. D. Belian, Geophys. Res. Lett. **25**, 3763 (1998).

[79] V. A. Sergeev, D. A. Yahnin, K. Liou, M. F. Thomsen, and G. D. Reeves, in *The Inner Magnetosphere: Physics and Modeling*, Geophysical Monograph Series Vol. 155, edited by T. I. Pulkkinen, N. A. Tsyganenko, and R. H. W. Friedel (American Geophysical Union, Washington DC, 2005), p. 55.

[80] D. L. Vainchtein, A. A. Vasiliev, and A. I. Neishtadt, Plasma Phys. Rep. **35**, 1021 (2009).

[81] A. Neishtadt, D. Vainchtein, and A. Vasiliev, Plasma Phys. Control. Fusion **53**, 085014 (2011).

[82] V. V. Zharkova, K. Arzner, A. O. Benz, P. Browning, C. Dauphin, A. G. Emslie, L. Fletcher, E. P. Kontar, G. Mann, M. Onofri, V. Petrosian, R. Turkmani, N. Vilmer, and L. Vlahos, Space Sci. Rev. **159**, 357 (2011).

[83] T. D. Phan, J. T. Gosling, M. S. Davis, R. M. Skoug, M. Øieroset, R. P. Lin, R. P. Lepping, D. J. McComas, C. W. Smith, H. Reme, and A. Balogh, Nature (London) **439**, 175 (2006).

[84] W.-L. Teh, B. U. Ö. Sonnerup, Q. Hu, and C. J. Farrugia, Ann. Geophys. **27**, 807 (2009).

[85] D. N. Baker, T. I. Pulkkinen, V. Angelopoulos, W. Baumjohann, and R. L. McPherron, J. Geophys. Res. **101**, 12975 (1996).

[86] J. Liu, V. Angelopoulos, A. Runov, and X.-Z. Zhou, J. Geophys. Res. **118**, 2000 (2013).

[87] J. Liu, V. Angelopoulos, X.-Z. Zhou, A. Runov, and Z. Yao, J. Geophys. Res. **118**, 7104 (2013).

[88] J. Kissinger, R. L. McPherron, T.-S. Hsu, and V. Angelopoulos, J. Geophys. Res. **117**, A05206 (2012).

[89] M. Fujimoto, T. Terasawa, T. Mukai, Y. Saito, T. Yamamoto, and S. Kokubun, J. Geophys. Res. **103**, 4391 (1998).

[90] A. V. Artemyev, A. A. Petrukovich, L. M. Zelenyi, R. Nakamura, H. V. Malova, and V. Y. Popov, Ann. Geophys. **27**, 4075 (2009).

[91] I. A. Daglis, R. M. Thorne, W. Baumjohann, and S. Orsini, Rev. Geophys. **37**, 407 (1999).

[92] K.-H. Glassmeier, S. Buchert, U. Motschmann, A. Korth, and A. Pedersen, Ann. Geophys. **17**, 338 (1999).

[93] L. Dai, K. Takahashi, J. R. Wygant, L. Chen, J. Bonnell, C. A. Cattell, S. Thaller, C. Kletzing, C. W. Smith, R. J. MacDowall, D. N. Baker, J. B. Blake, J. Fennell, S. Claudepierre, H. O. Funsten, G. D. Reeves, and H. E. Spence, Geophys. Res. Lett. **40**, 4127 (2013).

[94] T. I. Pulkkinen, D. N. Baker, C. J. Owen, J. T. Gosling, and N. Murphy, Geophys. Res. Lett. **20**, 2427 (1993).

[95] J. A. Slavin, E. J. Smith, D. G. Sibeck, D. N. Baker, and R. D. Zwickl, J. Geophys. Res. **90**, 10875 (1985).

[96] M. Hoshino, A. Nishida, T. Yamamoto, and S. Kokubun, Geophys. Res. Lett. **21**, 2935 (1994).

[97] Z. Vörös, Nonlin. Proc. Geophys. **18**, 861 (2011).

[98] M. Hoshino, A. Nishida, T. Mukai, Y. Saito, T. Yamamoto, and S. Kokubun, J. Geophys. Res. **101**, 24775 (1996).

[99] J. Šafránková, Z. Němeček, P. Cagaš, L. Přech, J. Pavlů, G. N. Zastenker, M. O. Riazantseva, and I. V. Koloskova, Astrophys. J. **778**, 25 (2013).

[100] T. Tanaka, Y. Saito, S. Yokota, K. Asamura, M. N. Nishino, H. Tsunakawa, H. Shibuya, M. Matsushima, H. Shimizu, F. Takahashi, M. Fujimoto, T. Mukai, and T. Terasawa, Geophys. Res. Lett. **36**, L22106 (2009).

[101] G. Kremser, R. Rasinkangas, P. Tanskanen, B. Wilken, and G. Gloeckler, Ann. Geophys. **12**, 152 (1994).

[102] S. Y. Fu, Q. G. Zong, T. A. Fritz, Z. Y. Pu, and B. Wilken, J. Geophys. Res. **107**, 1299 (2002).

[103] E. E. Grigorenko, L. M. Zelenyi, M. S. Dolgonosov, A. V. Artemiev, C. J. Owen, J.-A. Sauvaud, M. Hoshino, and M. Hirai, Space Sci. Rev. **164**, 133 (2011).

[104] J. A. Slavin, B. J. Anderson, D. N. Baker, M. Benna, S. A. Boardsen, R. E. Gold, G. C. Ho, S. M. Imber, H. Korth, S. M. Krimigis, R. L. McNutt, Jr., J. M. Raines, M. Sarantos, D. Schriver, S. C. Solomon, P. Trávníček, and T. H. Zurbuchen, J. Geophys. Res. **117**, A01215 (2012).

[105] B. J. Anderson, M. H. Acuña, H. Korth, M. E. Purucker, C. L. Johnson, J. A. Slavin, S. C. Solomon, and R. L. McNutt, Science **321**, 82 (2008).

[106] D. C. Delcourt, T. E. Moore, and M.-C. H. Fok, Ann. Geophys. **28**, 1467 (2010).
[107] J. A. Slavin, M. H. Acuña, B. J. Anderson, D. N. Baker, M. Benna, S. A. Boardsen, G. Gloeckler, R. E. Gold, G. C. Ho, H. Korth, S. M. Krimigis, R. L. McNutt, J. M. Raines, M. Sarantos, D. Schriver, S. C. Solomon, P. Trávníček, and T. H. Zurbuchen, Science **324**, 606 (2009).
[108] D. J. Gershman, J. A. Slavin, J. M. Raines, T. H. Zurbuchen, B. J. Anderson, H. Korth, D. N. Baker, and S. C. Solomon, Geophys. Res. Lett. **41**, 5740 (2014).
[109] L. Zelenyi, M. Oka, H. Malova, M. Fujimoto, D. Delcourt, and W. Baumjohann, Space Sci. Rev. **132**, 593 (2007).
[110] D. C. Delcourt, Ann. Geophys. **31**, 1673 (2013).
[111] A. V. Artemyev, I. Y. Vasko, and S. Kasahara, Planet. Space Sci. **96**, 133 (2014).
[112] C. T. Russell, K. K. Khurana, M. G. Kivelson, and D. E. Huddleston, Adv. Space Res. **26**, 1499 (2000).
[113] E. A. Kronberg, J. Woch, N. Krupp, A. Lagg, K. K. Khurana, and K.-H. Glassmeier, J. Geophys. Res. **110**, A03211 (2005).
[114] S. Kasahara, E. A. Kronberg, N. Krupp, T. Kimura, C. Tao, S. V. Badman, A. Retinò, and M. Fujimoto, J. Geophys. Res. **116**, A11219 (2011).
[115] L. A. Frank, W. R. Paterson, and K. K. Khurana, J. Geophys. Res. **107**, 1003 (2002).
[116] M. Kane, D. J. Williams, B. H. Mauk, R. W. McEntire, and E. C. Roelof, Geophys. Res. Lett. **26**, 5 (1999).
[117] J. L. Kohl, G. Noci, E. Antonucci, G. Tondello, M. C. E. Huber, L. D. Gardner, P. Nicolosi, L. Strachan, S. Fineschi, J. C. Raymond, M. Romoli, D. Spadaro, A. Panasyuk, O. H. W. Siegmund, C. Benna, A. Ciaravella, S. R. Cranmer, S. Giordano, M. Karovska, R. Martin, J. Michels, A. Modigliani, G. Naletto, C. Pernechele, G. Poletto, and P. L. Smith, Solar Phys. **175**, 613 (1997).
[118] R. Esser, S. Fineschi, D. Dobrzycka, S. R. Habbal, R. J. Edgar, J. C. Raymond, J. L. Kohl, and M. Guhathakurta, Astrophys. J. **510**, L63 (1999).
[119] J. F. Drake, P. A. Cassak, M. A. Shay, M. Swisdak, and E. Quataert, Astrophys. J. Lett. **700**, L16 (2009).
[120] Y. Li and J. Lin, Solar Phys. **279**, 91 (2012).
[121] E. Marsch, R. Schwenn, H. Rosenbauer, K.-H. Muehlhaeuser, W. Pilipp, and F. M. Neubauer, J. Geophys. Res. **87**, 52 (1982).
[122] E. Marsch, H. Rosenbauer, R. Schwenn, K.-H. Muehlhaeuser, and F. M. Neubauer, J. Geophys. Res. **87**, 35 (1982).